Pure Appl. Geophys. 171 (2014), 1219–1236
© 2013 Springer Basel
DOI 10.1007/s00024-013-0711-9

Pure and Applied Geophysics

Crustal Stress Map of Iran: Insight From Seismic and Geodetic Computations

Z. Zarifi,[1] F. Nilfouroushan,[1] and M. Raeesi[2]

Abstract—We used the focal mechanisms of crustal earthquakes (depth <40 km) in the period 1909–2012 and the available GPS velocities, derived from the data collected between 1999 to 2011, to estimate the magnitude and directions of maximum principal stress and strain rates in Iran. The Pearson product moment correlation was used to find the correlation between the stress field obtained from the focal mechanism stress inversion and that obtained using the seismic and geodetic strain rates. Our assumption is that stresses in a continuum are produced by tectonic forces and the consequent deformation on the crustal scale. Therefore, the direction of the stress and strain (or strain rate) are ideally to be the same. Our results show a strong correlation between the directions of the principal components of stress and strain (rate) obtained using the different data/methods. Using weighted average analysis, we present a new stress map for Iran.

Key words: Geodetic strain rate, seismic strain rate, stress inversion, Iran stress map.

1. Introduction

Many studies have associated the tectonics of Iran with the convergence of the Arabian and Eurasian plates. This convergence is mainly accommodated in the Zagros Mountains, in the west and the south west of Iran, Alborz and Kopeh Dag in the north and the north eastern part of Iran and the N–S strike slip faulting in eastern Iran (Fig. 1) (Jackson, 1992; Demets *et al*., 1994; Walker and Jackson, 2004). A few studies associated the tectonics of the Talesh region and northwestern Iran with the SW motion of the south Caspian basin with respect to Iran (e.g., Jackson *et al*., 2002). Recent global positioning system (GPS) studies have provided a precise distribution of deformation in Iran (Nilforoushan *et al*., 2003; Vernant *et al*., 2004a, b; Bayer *et al*., 2006; Hessami *et al*., 2006; Walpersdorf *et al*., 2006; Masson *et al*., 2006, 2007; Tavakoli *et al*., 2008; Peyret *et al*., 2009; Djamour *et al*., 2010, 2011; Mousavi *et al*., 2013). Following other studies (Papazachos and Kiratzi, 1992; Jackson *et al*., 1994; Kreemer *et al*., 2000), Masson *et al*. (2005) combined the geodetic strain rate field with the strain rate field deduced from seismicity to distinguish seismic from aseismic deformation in Iran using a non-uniform triangular mesh. Several other studies investigated the local or regional stress fields in Iran using a focal mechanism stress inversion of earthquakes in the Zagros (Gillard and Wyss, 1995; Lacombe *et al*., 2006; Navabpour *et al*., 2007, 2008), the Alborz (Zanchi *et al*., 2006) and the Kopeh Dag (Zamani *et al*., 2008).

Recent studies analyze different aspects of rupture propagation of earthquakes in geometrically complex fault systems to estimate the initiation, propagation and arrest of rupture (Sowers *et al*., 1994; Poliakov *et al*., 2002; Kame and Yamashita, 2003; Kame *et al*., 2003; Bhat *et al*., 2004; Fliss *et al*., 2005; Wesnousky, 2006). In all of these analyses the direction of maximum compression in the pre-existing stress field has a strong impact on the propensity of the rupture path to bend on to the potential branch path and to control the arrest or further propagation of rupture.

Besides providing an overall picture of the tectonic state of stress in Iran, knowledge of the geometrical complexities of the Iranian fault systems and of the direction of the pre-existing stress field

---

Electronic supplementary material The online version of this article (doi:10.1007/s00024-013-0711-9) contains supplementary material, which is available to authorized users.

[1] Department of Earth Sciences, Uppsala University, Villavägen 16, 75236 Uppsala, Sweden. E-mail: zoya.zarifi@geo.uu.se; faramarz.nilfouroushan@geo.uu.se

[2] Department of Earth Science, University of Bergen, Allegaten 41, 5007 Bergen, Norway. E-mail: Mohammad.Raeesi@geo.uib.no

Birkhäuser

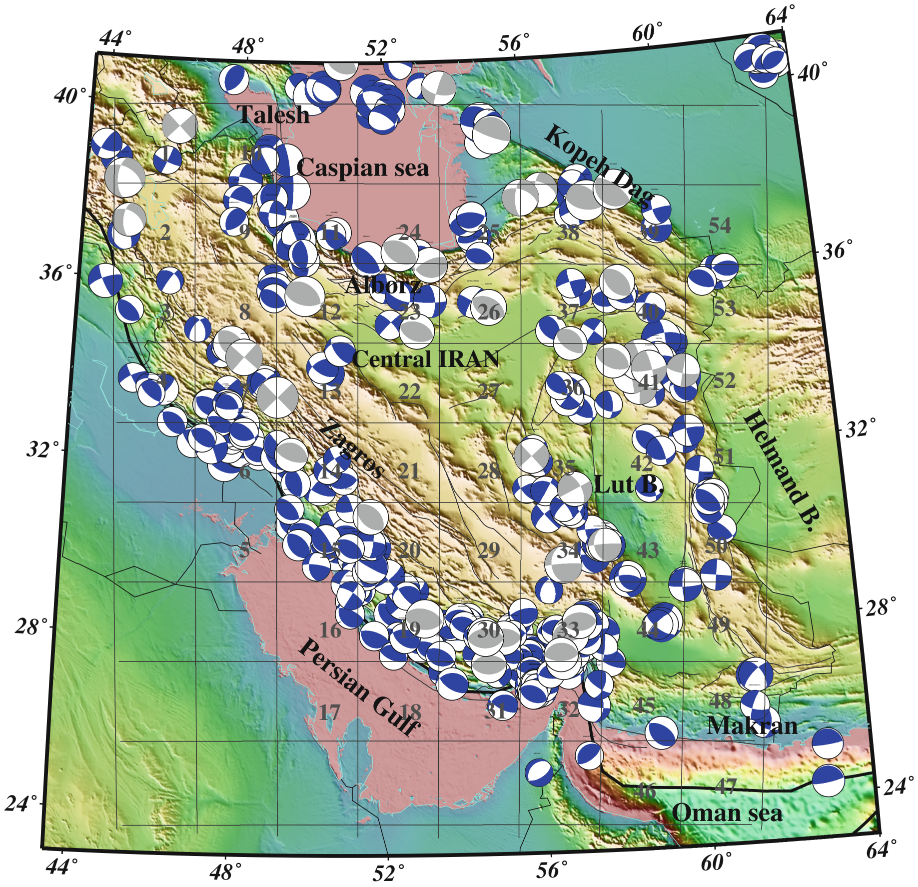

Figure 1
Focal mechanism of earthquakes in Iran in the period 1909–2011. The gray mechanisms are from Jackson *et al*. (1995) and the blue ones from the global CMT catalog. 200 km × 200 km cells are used, and these are sequentially numbered starting from 1 in the northwest corner to 54 in the northeast of Iran

may also significantly improve hazard assessments in populated areas. From the time of the Damghan earthquake (22 December 865, M7.9) to the recent twin earthquakes in Tabriz (11 August 2012, M6.3 and M6.4), Iran has suffered with more than 664,000 fatalities due to earthquakes (official reports). Our aim, in this paper, is to use all available geodetic data (1999–2011) and focal mechanism of earthquakes (1909–2012) to determine a stress map of Iran. If we assume that stresses in a continuum are produced by the application of tectonic forces and its consequent deformation on the crustal scale, then the direction of the principal components of the stress and strain (or strain rate) tensors must ideally be the same. In the next three sections we present the analysis of the various seismic and geodetic data. We then combine these multidisciplinary data to produce the stress map. This stress map is then used to discuss the various tectonic regimes in Iran.

2. *Focal Mechanism Stress Inversion (FMSI)*

According to McKenzie (1969), the crustal stress tensor cannot be estimated with confidence by relying on the focal mechanism of only one earthquake. Instead, one needs an inversion technique to estimate the stress tensor from a larger number of earthquakes in a region. Here, we used focal mechanism stress inversion (FMSI) as described by Michael (1984, 1987, 1991) (ZMAP software [Wyss, 2001]) to derive the spatially uniform time-averaged components of the stress field in Iran. The stress tensor is described by the three orthogonal orientations of the three principal stresses σ_1, σ_2 and σ_3 and a relative measure of stress, the stress ratio which is defined by $\varphi = \frac{(\sigma_1 - \sigma_2)}{\sigma_s - \sigma_1}$, and which represents the shape of a deviatoric ellipsoid. The calculation of the variance shows how well the result fit to a homogeneous stress field. In order to find the 95 % confidence region, the method finds 95 % of the stress tensors that are closest to the best value based on the normalized scalar product of two stress tensors according to the Eq.:

$$\frac{\sum_{i=1}^{3}\sum_{j=1}^{3} M_{ij}N_{ij}}{\left(\sum_{i=1}^{3}\sum_{j=1}^{3} M_{ij}^2\right)^{0.5}\left(\sum_{i=1}^{3}\sum_{j=1}^{3} N_{ij}^2\right)^{0.5}}. \qquad (1)$$

Here the components of the two stress tensors M and N are denoted by M_{ij} and $N_{ij,}$ respectively.

3. Earthquake Data and FMSI Results

Since the main assumption in the stress inversion is that the stress field is uniform in each cell, we generated a mesh assuming that different patterns of faulting can be observed in each cell.

Table 1

Result of the focal mechanism stress inversion (FMSI)

Cell	σ_1		σ_2		σ_3		Variance	φ
	Azimuth	Rake	Azimuth	Rake	Azimuth	Rake		
4	46.9	14.8	137.3	1.9	−125.6	75	0.11	0.47
6	22.6	1.7	−67.6	8.3	123.9	81.4	0.051	0.25
7	21.7	6.4	−179	83.1	−68.5	2.4	0.048	0.42
8	−82.1	8.5	10.6	17.6	163	70.3	0.059	0.59
9	−29.3	13.2	−130.1	38.8	75.9	48.1	0.098	0.42
10	−65.3	35.4	13.6	53.3	30.5	8.2	0.14	0.45
11	−106.1	4.9	161.4	24.6	−5.7	64.7	0.13	0.16
14	13.3	1.8	−77.4	22.3	107.7	67.7	0.073	0.31
15	−142.1	2.3	118.7	75.3	−51.6	14.5	0.049	0.19
16	50.4	11.3	−172.4	74.6	−41.6	10.2	0.043	0.4219
19	−155.8	5.1	−56.8	60.8	111.2	28.6	0.043	0.82
20	37.6	8.5	−160.6	81	−52	2.8	0.056	0.32
23	−161.1	23.8	50.9	62.4	−65.3	13	0.21	0.41
24	93.2	6.3	2.2	9.2	−142.6	78.8	0.04	0.24
25	−9.4	2.8	−100.3	18.3	88.9	71.4	0.041	0.37
26	20.6	42	111.2	0.7	−157.9	48	0.047	0.9
30	8.8	1.7	−81.6	12.7	106	77.1	0.11	0.23
31	170.2	16	55.1	55.9	−90.4	29.1	0.016	0.31
32	−6.2	7.6	84.7	7	−143.2	79.6	0.038	0.45
33	−5.7	6.1	97.5	65	−98.4	24.1	0.071	0.12
34	11.4	18.5	107.5	17.6	−121.8	63.9	0.026	0.72
35	0.5	1.2	−97.8	81.5	90.6	8.4	0.049	0.31
36	57.8	11.3	−54.7	63.2	153	24.8	0.045	0.21
39	38.7	14.1	−108.8	73.3	130.8	8.6	0.021	0.28
40	48.6	1.8	−42.2	25	142.4	64.8	0.11	0.26
41	−137.8	3.7	−40.1	64.3	130.2	25.4	0.023	0.11
43	−151.8	10.3	−40.1	63.9	113.5	23.6	0.032	0.23
44	−102.1	11.2	−3.4	37.6	154	50.1	0.15	0.61
45	42	7.2	−58.4	54.9	136.9	34	0.054	0.16
48	−113.8	19.3	113.2	62.7	−17.2	18.4	0.0021	0.32
50	−130.5	6.3	138.1	10.5	−10	77.6	0.013	0.18
51	−132.8	5.5	4.8	82.6	136.5	4.9	0.0053	0.47
53	−118.8	25.7	34.8	54.2	145.2	35.8	0.0052	0.39

Data are obtained from the global CMT catalogue and Jackson *et al*. (1995). Minimum number of earthquakes used to obtain FMSI is three

Having a different geometry and pattern for faulting, one can estimate the average of spatial stress field in different cells. In this study we use a uniform mesh, with square cells (200 km × 200 km) that are wide enough to assure the existence of complexity in the pattern of faulting in each cell and, at the same time, allows for the possible variation of the state of stress between adjacent cells.

We compute the stress field in each cell, using the focal mechanism of crustal earthquakes (shallower than 40 km). We use two data sets. The first dataset is based on Jackson *et al*. (1995) and covers the period 1909–1976. The second dataset uses the global CMT catalog and covers the period 1977–2012. Many of the focal mechanisms derived by Jackson *et al.* (1995) are based on surface faulting which were accompanied by these events. The spatial distribution of the focal mechanisms used in this study is shown in Fig. 1. This figure clearly shows that most of the focal mechanisms are concentrated in the Zagros, Alborz, Kopeh Dagh and Talesh Mountains and around the Lut block in eastern Iran. The main assumption of FMSI is that a perturbation in the stress field as a result of different sources of heterogeneity can be neglected with respect to the regional stress field. This assumption is valid if a large number of data are used. However, this is not always the case. In particular, in our inversion in a number of cells (cells 10, 16, 24, 26, 45, 48 and 53), the number of events was as low as 3. The FMSI results are presented in Table 1 and Fig. 2. It is important to note; however,

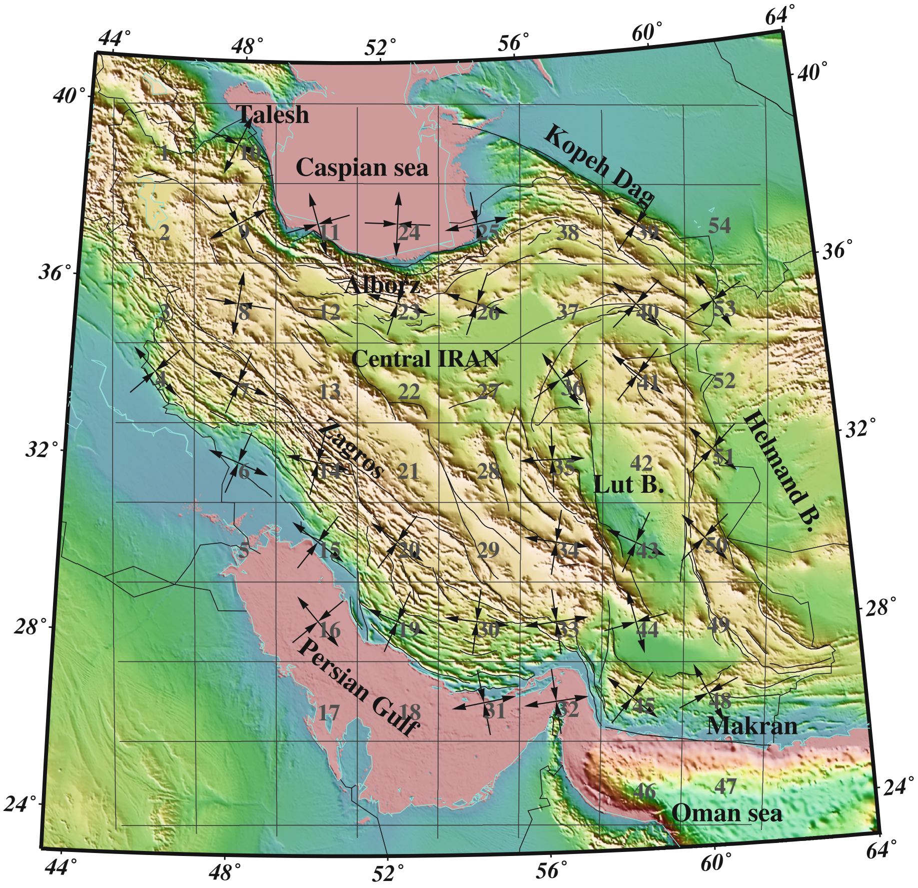

Figure 2

Direction of maximum principal axes of compressional and extensional stresses obtained from FMSI. *Empty cells* indicate that there were not enough data that one of the main objectives of this study is to compare and combine these results with the seismic and geodetic inversions.

Figure 3 shows the FMSI result for each cell with a 95 % confidence limit. As can be seen from Fig. 3, the low seismicity in cells 10, 16, 24, 26, 45, 48 and 53 could give rise to areas with low confidence limits. The results show the distinct tectonic settings of Iran. A northeastward compression along the Makran subduction zone changes to a northwestward compression in the transition zone between the Makran subduction zone and the Zagros collision zone, while to the west of the Zagros belt, the direction of compression changes towards the northeast. The dominant direction of compression in eastern Iran and along the Kopeh Dag is towards the northeast, which is in agreement with the direction of compression east of the southern Alborz mountain range. However, in the southern Caspian Sea and the northern Alborz, this direction is rotated to almost east–west. The compressional axis of stress changes its direction again in the Talesh region, in northwestern Iran, towards the northwest.

4. *Seismic Strain Rate (SSR)*

In a seismically active region like Iran, earthquakes are related to many faults which are complex in geometry and are distributed irregularly. In such cases, the tectonic process can be described by its deformation rate, where fractures at the source are assumed to be randomly distributed (Kostrov, 1974; Kostrov and Das, 2005). In order to calculate the components of the strain rate tensor, we used Kostrov (1974) formulation in each cell:

$$\dot{\varepsilon}_{ij} = \frac{1}{2\mu V}\sum_{n=1}^{N} M_{ij}^{n}. \tag{2}$$

Here, μ is the modulus of rigidity and M_{ij}^{n} is the ij-the component of the moment tensor of earthquake n with scalar moment M_0 and $\hat{n}$, the unit normal vector to the fault plane and $\hat{d}$, the unit slip vector, with $M_{ij} = M_0\left(n_i d_j + n_j d_i\right)$ (Stein and Wysession, 2001). Here the assumption is that earthquakes have occurred in volume V and over a time interval of t. We assume a continental crustal rigidity of $\mu = 3 \times 10^{10}$ Pa and a seismogenic thickness of 15 km as estimated by other studies (Jackson and McKenzie, 1988; Hatzfeld *et al.*, 2003; Talebian and Jackson, 2004).

5. *SSR Results*

The same data and grid that were used in FMSI, have been used to calculate the SSR. Table 2 and Fig. 4 present the direction and magnitude of the principal axes of seismic strain rate obtained from Eq. 2. The magnitude of the seismic strain rates illustrates the variable rate of deformation in different cells as well as the dominant state of deformational regime in terms of compression or extension. Figure 4 shows that, in Zagros, the seismic strain rate obtains its highest value in cell 7 in the northwestern part of Zagros with a predominantly compressional deformation regime (compare the size of the red and blue circles, representing the magnitude of compression and extension, respectively). In the other regions, most of the seismic deformation derived from modern seismicity, is related to eastern Iran and the southwestern Caspian Sea (NW Alborz). In neighboring cells of 44 and 33, as well as in cells 41 and 36, the dominant deformation regime changes abruptly from compression to extension. The other peculiar feature is the dominant extensional strain, observed in cells 19 and 30, in the collision zone between Arabian and Eurasian plates.

6. *Combination of GPS Velocities*

The GPS velocities are usually estimated either in regional or global reference frames based on the extent of the network and its application. In geodesy, global reference frames such as International Terrestrial Reference Frames (ITRFs) are generally of interest and in tectonic studies stable-plate frames, such as Eurasia-fixed, are more suitable to study relative plate movements or to detect movements around active faults.

In recent years, the active tectonic deformation of Iran has been constrained by several geodetic studies using either campaign-mode surveys or/and permanent GPS stations (Nilforoushan *et al.*, 2003; Vernant *et al.*, 2004a, b; Bayer *et al.*, 2006; Hessami *et al.*, 2006;

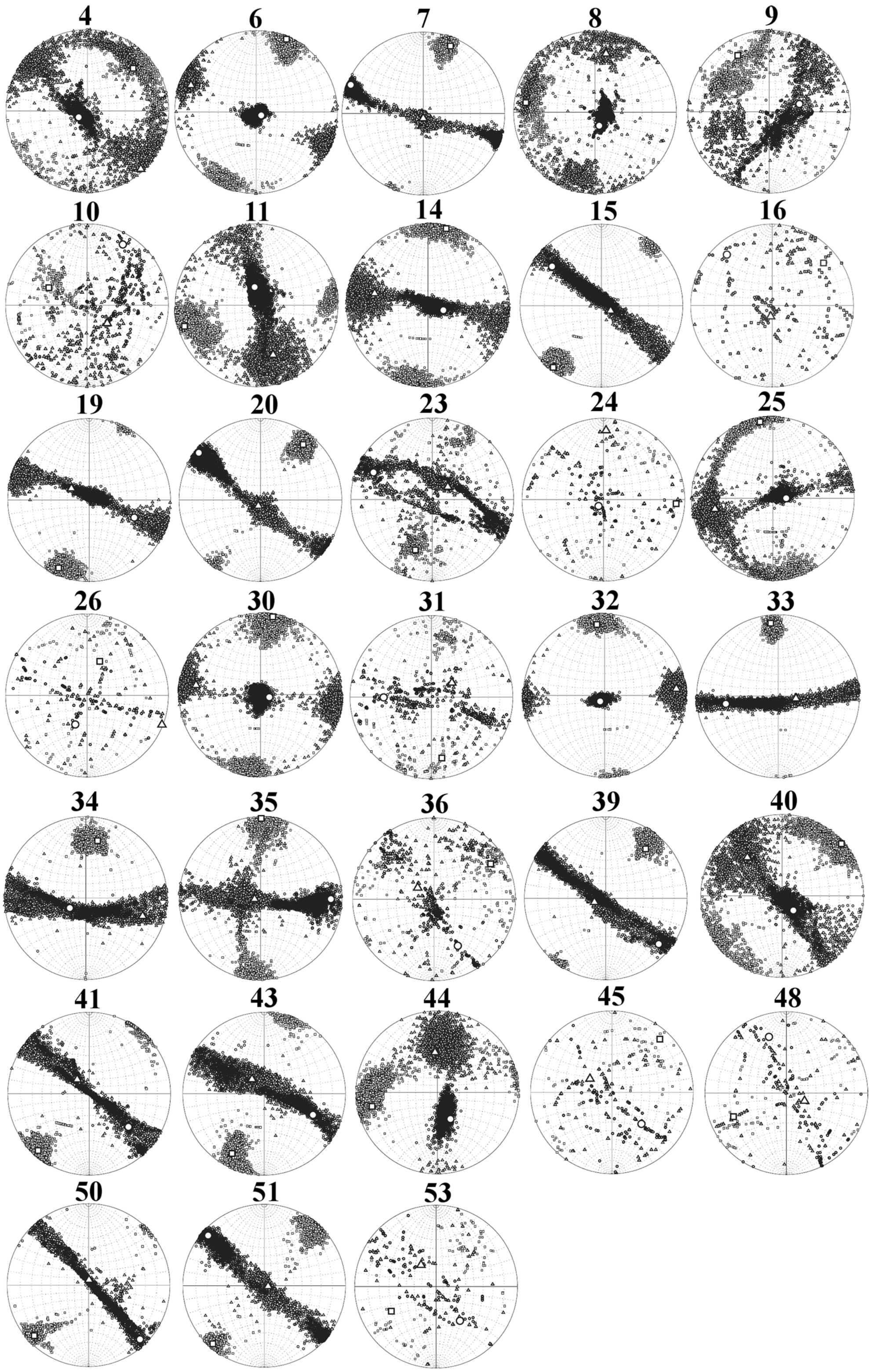
4
6
7
8
9
10
11
14
15
16
19
20
23
24
25
26
30
31
32
33
34
35
36
39
40
41
43
44
45
48
50
51
53

◀

Figure 3
Results of FMSI in each cell with 95 % confidence level. The three principal axes of σ_1, σ_2 and σ_3 are represented by a *big open square*, a *circle* and a *triangle*, respectively. Wulff nets with expanded area of confidence levels represent a relatively poor fit to a homogenous stress field

Table 2

Principal axes of seismic strain rate obtained in this study in 10^{-10} *year*$^{-1}$

Cell	$\dot{\varepsilon}_1$ (compressional)	$\dot{\varepsilon}_2$ (extensional)	Azimuth of $\dot{\varepsilon}_1$
4	−0.625	0.342	79.5
6	−5.214	0.749	83.7
7	−4.93	24.1	44.4
8	−29.04	3.56	45.2
9	−11.47	11.28	−36.0
10	−5.360	3.70	−8.9
11	−374	375	54.6
14	−5.734	6.097	40.4
15	−4.796	0.651	6.3
16	−0.405	0.364	50.6
19	−1.08	84.57	59.7
20	−12.77	6.28	72.6
23	−12.35	0.04	52.5
24	−63.8	70.30	88.2
25	−14.2	14.7	−11.4
26	−27.7	1.6	17
30	0.1	49.72	11
31	−1.31	0.26	−27.3
32	−6.77	1.32	−47
33	−98.09	15.46	36.9
34	−42.19	0.8	13.5
35	−7.65	1.67	16.3
36	−363	0.9	28.26
39	−516	575	34.6
40	−17.04	17.26	84
41	−14.6	455	25.94
43	−224	234	45.50
44	−2.0	71.7	29.7
45	−2.73	4.21	39
48	−21.57	22.19	28.3
50	−6.43	8.22	65.6
51	−5.09	5.70	36.5
53	−128	128	60.8

The Azimuth of $\dot{\varepsilon}_1$ is in degrees

Walpersdorf *et al.*, 2006; Masson *et al.*, 2006, 2007; Tavakoli *et al.*, 2008; Peyret *et al.*, 2009; Djamour *et al.*, 2010, 2011; Mousavi *et al.*, 2013). Because each individual velocity solution was obtained by different processing strategies, or by choosing a different reference frame, the published GPS velocities cannot be directly merged, even if they are declared or are transformed in the same reference frame. For example, the velocity differences computed for common stations between the solutions in the Eurasia-fixed frame were 1–3 mm/year, which later, after using transformation parameters between solutions, improved to 0.5 mm/year (see below for details). Therefore, the first important step for combination is to unify the reference frames by mathematical methods and generate a combined velocity field in that unified frame (e.g., Dong *et al.*, 1998, Nocquet, 2012).

We used the VELROT program, version 1.01 (Herring *et al.*, 2010) to compare and combine the velocity fields by estimating translation and rotation parameters between them. In order to combine the velocity fields using VELROT, we only chose those solutions which had enough common stations in Iran and also those solutions for which the residual velocities computed for common stations during transformation was below 1 mm/year. Therefore, we did not take into account Hessami *et al.* (2006) and Peyret (2009) due to lack of enough and good common stations with other solutions. We also ignored solutions by Nilforoushan *et al.* (2003), Vernant *et al.* (2004a, b) and Masson *et al.* (2006), but used the latest solutions by Djamour *et al.* (2010, 2011) and Masson *et al.* (2007) instead, as these had observed the same stations but with longer time spans and more surveys, thus providing more reliable velocities. Finally, we used the velocity fields of Bayer *et al.* (2006), Masson *et al.* (2007), Walpersdorf *et al.* (2006), Tavakoli *et al.* (2008), Djamour *et al.* (2010, 2011) and Mousavi *et al.* (2013). These solutions reported their velocity fields either in ITRF or/and in Arabia-fixed or/and in Eurasia-fixed frames. The different ITRF realizations (ITRF2000, ITRF2005 and the latest one, ITRF2008) used in these studies were noted for velocity combinations. Supplementary Table A1 shows the combination steps, input solutions for each step, input and target reference frames, and the RMS of the velocity residuals. The small RMS values in Supplementary Table A1 show the good agreement between different solutions (about 0.5 mm/year). The final combined velocity solution is listed in Supplementary Table A2 and shown in Fig. 5 and is used for the geodetic strain rate estimations.

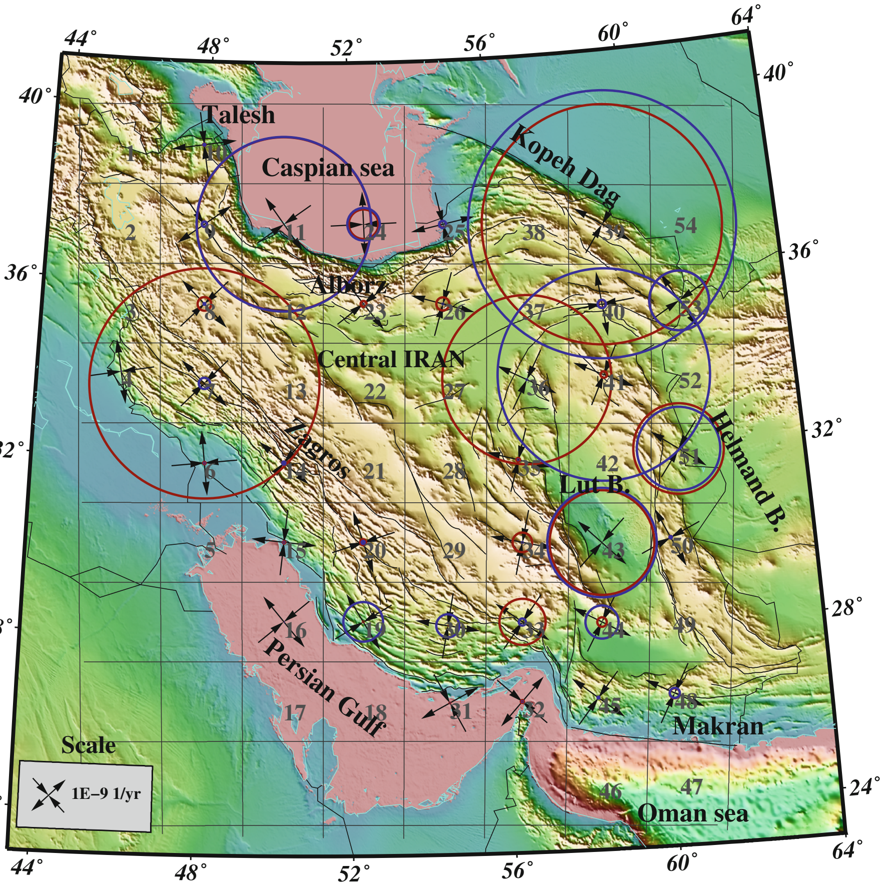

Figure 4

Direction and relative magnitude of principal axes of seismic strain rate in Iran (see also Table 2). The *blue circles* represent magnitude of extensional strain. The *red circles* represent magnitude of the compressional strain rate. In some cells, extension (cells 41, 44, 19 and 30) or compression (7 and 36) are the dominant regime

7. *GPS-derived Strain Rates (GSR)*

We used the SSPX program (Cardozo and Allmendinger, 2009) to compute the infinitesimal horizontal strain rates from GPS horizontal velocities with the same grid pattern as FMSI and SSR. The SSPX program and its predecessor Strain SimPro have been successfully used in previous studies for deformation analysis of GPS networks (Allmendinger *et al.*, 2005, 2007; Mullick *et al.*, 2009; Unglert *et al.*, 2011). This program is able to calculate strain and strain rates from 2D and 3D displacement and velocity data; and it can compute all deformation parameters. Out of the seven different methods in SSPX to compute the strain or strain rates, we used the Grid-Distance Neighbor method. Since our GPS stations are not uniformly distributed and we are dealing with heterogeneous tectonic deformation in our study area, the Grid-Distance Neighbor method works well and produces a more meaningful solution (Allmendinger *et al.*, 2007). The Grid-Distance Neighbor method uses weighted least squared adjustment where each station is weighted by its distance to the center of the cell:

$$W = \exp\left(\frac{-d^2}{2\alpha^2}\right), \tag{3}$$

where W is the weighting factor, d is the distance and α is a constant that specifies how the closeness of the stations to the center of the cell influences the strain solution. Stations within 1α distance contribute more than 67 % to the solution whereas those at a distance

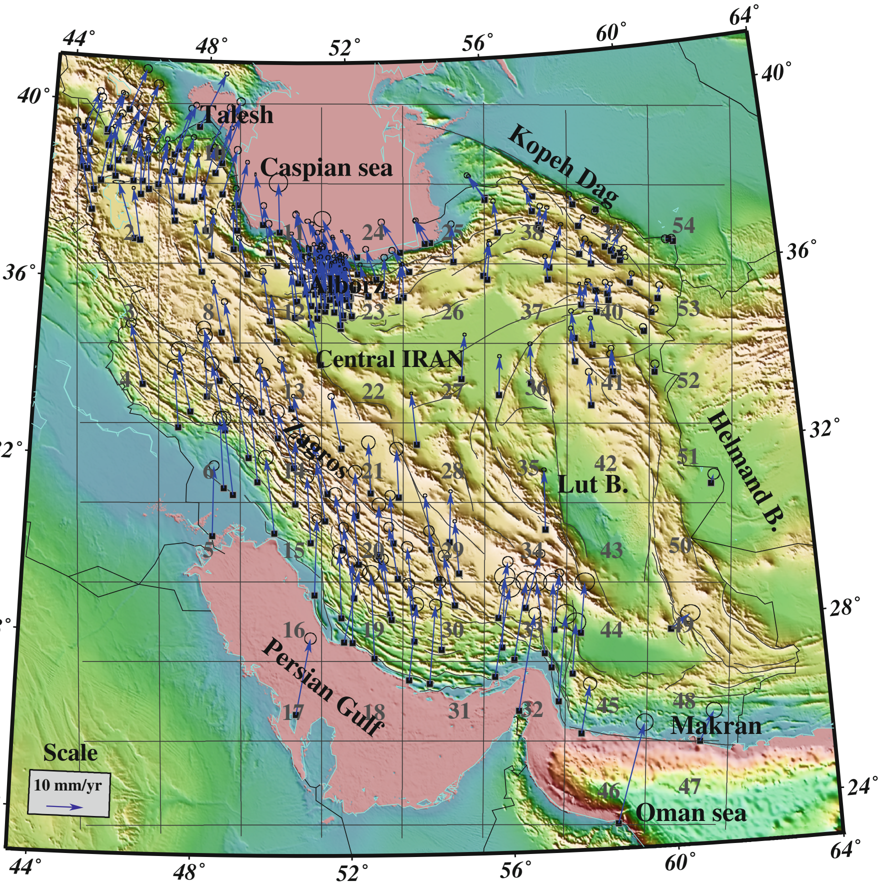

Figure 5
GPS stations (*black rectangles*) and the combined velocity field with their error ellipses in the Eurasian fixed reference frame (EURA_I08). The combined velocity field is listed in Supplementary Table A2 and based on Bayer *et al.* (2006), Masson *et al.* (2007), Walpersdorf *et al.* (2006), Tavakoli *et al.* (2008), Djamour *et al.* (2010, 2011), and Mousavi *et al.* (2013)

greater than 3α contribute <1 % (Cardozo and Allmendinger, 2009). In contrast to the Delaunay triangulation method where strain rates are estimated at the center of the non-equal area triangles formed by the non-equally spaced GPS stations; it gives more reasonable results and better visualization of the strain rate directions and magnitudes on an equal-area regular grid. Of course, the small station spacing and active deformation results in very high strain rates if no distance-weighted factor is used (Cardozo and Allmendinger, 2009).

We estimated the strain rates at the center of each cell of a 200 × 200 km rectangular grid by inclusion of 239 Eurasia-fixed GPS velocities (Fig. 5), Grid-Distance Neighbor method and $\alpha = 150$ km (see Allmendinger *et al.,* 2007). As discussed earlier, the Grid-Distance Neighbor method, the velocity of the close stations contribute more to the solutions, and; therefore, a more reasonable strain rate field is estimated for such a heterogeneous tectonic region where different kinematics and deformation mechanisms are observed (e.g., Nilforoushan *et al.,* 2003; Allmendinger *et al.,* 2007). Figure 6 and Table 3 show the results of our geodetic strain rate computation for Iran. According to the geodetic observations, the northeastward shortening is the dominant deformational regime in the southern, southwestern, eastern and northeastern parts of Iran. The deviation from this general trend can be seen only in northwestern Zagros as well as the northwestern part of Iran, in the Talesh region. In general there is a good agreement

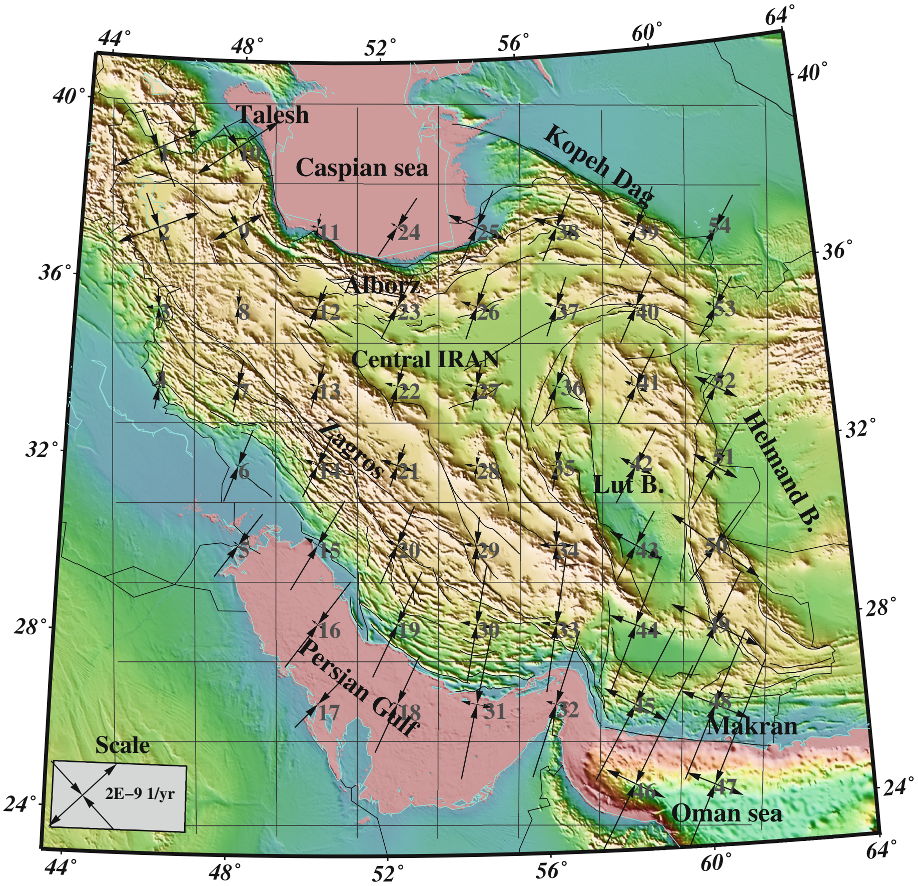

Figure 6
Principal geodetic strain rates derived from combined GPS velocities

between the direction of the principal axes of geodetic strain and what has been computed by seismic strain and/or stress inversion of focal mechanisms except in the Zagros–Makran transition zone and the southern part of the Caspian Sea. In the next section, we compare the results obtained from the different methods used in this study and integrate them to present a new stress field for our study area.

8. *Stress and Strain Analyses in Iran*

In order to obtain the best model to describe the directions of principal axes of stress in Iran, we compare the results of FMSI with those obtained using seismic and geodetic data. The notion is that stresses in a continuum are produced by the application of tectonic forces and its consequent deformation in the crustal scale. Therefore, the direction of the principal axes of the stress and strain (or strain rate) tensors must ideally be the same. Figure 7 shows a comparison between the direction of the maximum principal stress and seismic/geodetic strain rates in Iran.

We calculated the Pearson product moment correlation between the obtained results from stress inversion of focal mechanisms with what we obtained from geodetic and seismic strain rate tensors. The Pearson's correlation coefficient between two sets of variables is defined as the covariance of the two variables cov(x, y) divided by the product of their standard deviations (σ_x and σ_y) (e.g. Gibons, 1982) as given by:

$$\rho_{xy} = \frac{\mathrm{cov}(x, y)}{\sigma_x \sigma_y}. \tag{4}$$

The Pearson's correlation coefficient defined in this equation is a measure for the amount of linear correlation between the two data sets. Pearson's density (ρ) varies from −1 to +1, where $\rho = +1$ suggests a perfect positive linear relationship between the two sets of variables. Our results show a strong correlation between the obtained stress tensor and strain tensor analysis in this study, with $\rho = +0.84$ the correlation value for the data derived using FMSI and SSR, $\rho = +0.78$ the correlation value for SSR and GSR and $\rho = +0.79$ the correlation value for FMSI and GSR. We also calculated the mean direction of compressional stress (and strain rate) in each cell and the absolute value of deviation of each method of analyzing of stress/strain tensor from this mean value. We present a new directional stress field in Iran, by using the following weighted average:

$$\mathrm{Weighted}_{\mathrm{AVE}} = \frac{\mathrm{Coef}_{\mathrm{FMSI}} \times \mathrm{FMSI} + \mathrm{Coef}_{\mathrm{SSR}} \times \mathrm{SSR} + \mathrm{Coef}_{\mathrm{GSR}} \times \mathrm{GSR}}{\mathrm{Coef}_{\mathrm{FMSI}} + \mathrm{Coef}_{\mathrm{SSR}} + \mathrm{Coef}_{\mathrm{GSR}}} \quad (5)$$

$$\mathrm{Coef}_{\mathrm{Method}} = \frac{\sum \mathrm{Dev.Methods} - |\mathrm{Dev.from\ mean\ method}|}{\sum \mathrm{Dev\ methods}} \quad (6)$$

$$\sum \mathrm{Dev.\ methods} = |\mathrm{Dev.\ from\ mean\ FMSI}| + |\mathrm{Dev.\ from\ mean\ SSR}| + |\mathrm{Dev.\ from\ mean\ GSR}|. \quad (7)$$

Here | | denotes the absolute value and "Dev. from mean FMSI" is the deviation of the FMSI result in the cell from the mean value of the three methods, representing the direction of stress, in that cell. Here, the highest weight is associated with the method with least deviation from the mean value and the lowest weight is assigned to the method with highest deviation from the mean value. The results of our statistical approach are presented in Table 4. Figure 8 shows the direction of weighted average compressional stress in Iran.

9. *Results and Discussion*

A combination of several GPS velocity fields extracted form previous studies and the resulting strain-rate field has helped us to better illustrate the present-day active deformation in Iran. The relatively dense network of GPS stations in Zagros, Alborz, NW and NE Iran (Fig. 5) provided more accurate and reliable solutions for geodetic strain analysis. The gridding of the non-uniformly distributed GPS velocities in our study area also helped us to infer the local deformation in the areas where no (or a few) GPS stations exist at our 200 km grid resolution. However, in order to provide more accurate constraints on such complex tectonically deforming zones in the center and eastern part of Iran, such gaps should be filled by installation and observation of more GPS stations.

The combination of results from geodetic measurements, seismic strain rates and focal mechanism stress inversion and their robust correlation, provides a stress map in Iran based on a multi-disciplinary approach, which should be helpful in explaining the general tectonic setting of the Iranian Plateau.

The magnitude of the GPS principal strain rate components and the topography of the study area in Fig. 6 show that the present-day deformation in most parts of Iran is mainly compressional. Generally the compressional strain rate components are perpendicular to the fold axes and thrust faults (Fig. 6). The computed strain rate magnitudes and directions change based on the tectonic activity of the local area defined by the grid cells. Relatively large compressional components of geodetic strain rate are observed in southeastern Iran, the Makran region and the coastal area of Oman sea, (cells 45, 46 and 47; Fig. 6) where oceanic crust of Arabian plate subducts beneath Eurasian plate (NILFOROUSHAN *et al.*, 2003;

Masson *et al.*, 2007). The lack of seismic activity near the coast of the Oman Sea is the reason that we did not determine a seismic strain rate in this area. There are two possible explanations for this lack of seismic activity. First, the strain accumulates at the slab interface, which can give rise to future big earthquakes, or secondly, there is a free slip condition in the westernmost part of the Makran subduction zone. A study by Zarifi (2007) gives clear evidence of strong coupling in the western Makran. In addition, according to Stern (2002), observations of compressional stress in the back arc of the subduction zones (here, cells 45, 48, 44 and 49) confirm strong coupling at the slab interface. Therefore, geodetic measurements in the cells associated with the back arc of Marakan, with a strong compressional component may be evidence of strong coupling at the slab interface. However, this contradicts the result from the seismic strain rate inversion. Despite good agreement in the directions of the principal stress and strain axes in cells 44 and 48, the magnitude of the compressional and extensional strain rates show a strong mismatch between the geodetically measured and the seismically computed values (see Figs. 4, 6). We explain this mismatch with the short time span of the geodetic data in the region and also the occurrence of ‘old’ strike slip earthquakes in the overriding plate in Makran. The trend and mechanism of faulting in cells 44 and 48 (Figs. 1, 4) show strike slip faults with fault planes perpendicular to the direction of compression and may confirm stress partitioning in this area, where there is an overriding lithosphere. The rotation of the Arabian plate relative to the Eurasian plate, which is accommodated by active subduction at the Makran trench (Bellahsen *et al.*, 2003; Reilinger *et al.*, 2006), can explain the possible stress partitioning in the overriding lithosphere. Indeed, Bayer *et al.* (2006) and Peyret *et al.* (2009) have associated the big component of geodetic extension rate (2e$-$8 s^{-1}), in their study, in the westernmost Makran (cells 45 and 46) to the strike-slip components of Minab–Zendan fault. The shortening direction in those cells has an average 30° orientation towards NNE. These shortening orientations based on geodetic measurements change slightly and based on seismic observations (FMSI)

Table 3

Principal axes of geodetic strain rates obtained in this study in 10^{-10} *year*$^{-1}$

Cell	$\dot{\varepsilon}_1$ (compressional)	$\dot{\varepsilon}_2$ (extensional)	Azimuth of $\dot{\varepsilon}_1$
1	−180.96	201.25	334.04
2	−157.29	187.37	337.23
3	−80.65	60.23	356.16
4	−97.96	34.77	8.74
5	−169.21	28.38	36.62
6	−165.41	13.37	21.14
7	−113.87	26.41	10.05
8	−75.39	6.88	1.85
9	−88.15	122.43	330.44
10	−118.28	210	325.62
11	−59.48	−35.35	10.84
12	−97.76	10.25	21.59
13	−100.08	40.72	16
14	−150.32	64.87	25.28
15	−224.66	69.88	31.06
16	−231.51	33.74	37.41
17	−140.57	−5.97	44.66
18	−227.75	22.03	25.35
19	−250.02	23.62	25.84
20	−182.28	55.80	24.16
21	−98.01	78.98	20.37
22	−97.24	59.28	16.32
23	−155	62.79	27.66
24	−148.94	32.75	34.58
25	−171.46	138.74	25.91
26	−147.97	75.09	20.92
27	−102.61	52.63	12.79
28	−61.27	53.36	8.47
29	−121.88	58.39	7.04
30	−254.97	74.02	11
31	−327.87	69.88	13.05
32	−328.48	48.29	20.01
33	−291.52	69.09	10.60
34	−106	77.25	4.01
35	−110.70	26.79	11.56
36	−138.50	24.51	21.75
37	−133.28	54.74	21.13
38	−156.59	113.65	25.77
39	−188.8	75	26.63
40	−167.69	55.87	27.76
41	−179.52	58.22	30.35
42	−181.74	80.64	31.93
43	−166.17	131.1	32.19
44	−315.57	122.4	24.01
45	−368.21	154	30.81
46	−566.06	142.17	28.83
47	−576.10	132.73	25.69
48	−346.45	159.77	26.02
49	−253.07	212.11	29.96
50	−187.50	234.69	40.77
51	−210.13	111.76	34.06
52	−185.95	105.81	31.63
53	−147.94	51.67	33.77
54	−157.84	23.16	34.06

The Azimuth of $\dot{\varepsilon}_1$ is in degrees

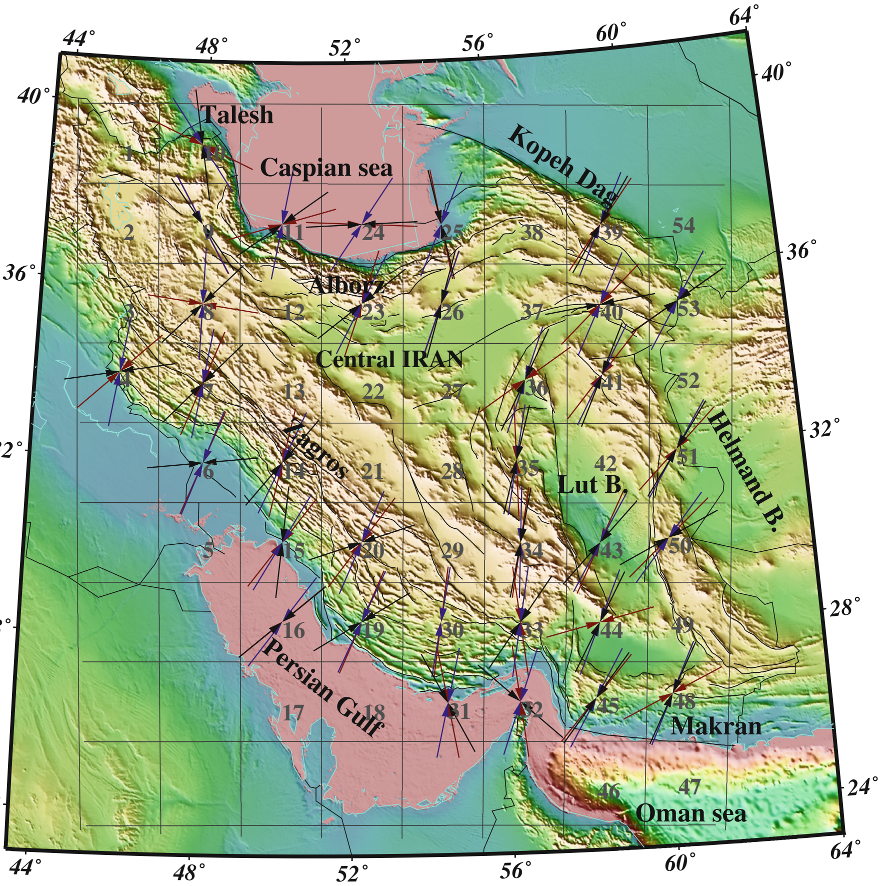

Figure 7
Comparison between direction of principal axes of stress (*red*) and seismic (*black*)/geodetic (*blue*) strain rates in Iran. If not enough earthquake data are available for a cell, then that cell is left empty

significantly anticlockwise in Makran–Zagros transition (cells 32, 33) where a transition from oceanic-continental subduction in Makran to continental–continental collision in Zagros takes place (Bayer *et al.,* 2006; Peyret *et al.,* 2009; Regard *et al.,* 2004). Seismic strain rates in adjacent cells 34, 33 and 44 show that the transition zone between Makran and Zagros can significantly affect the dominant stress field in the area. The predominantly extensional regime on the Makran side, (cell 44), is replaced by a predominantly compressional regime on the Zagros side (cells 33, 34). Compression is the dominant regime in most areas of Zagros (see Figs. 4, 6) except cells 19 and 30 (based on seismic strain rate analysis). This extensional regime could be due to the presence of a 1–2 km thick salt layer under the cover sediments where this mechanically weak salt layer eases the fan-shaped deformation distribution in the southeastern part of the Zagros (Nilforoushan and Koyi, 2007).

Geodetic and seismic calculations (GSR, SSR and FMSI) confirm the heterogeneous deformation in terms of both magnitude and direction at Zagros. The clear strain partitioning in the Zagros fold-thrust belt is observed from the south to the northwest. An almost orthogonal shortening of the belt (shortening perpendicular to the geological structures and strike of the belt) in cells 33, 30, 31, 19, 20, 21, 15 and 14 is observed whereas the shortening direction is rotating anticlockwise as derived from geodetic measurements and focal mechanism stress inversion in the northwestern part of the belt and trends obliquely to the strike of the belt (cells 14, 6 and 7) (Figs. 3, 6 and 7). This observation has also been reported by previous studies (Hessami *et al.,* 2006; Walpersdorf *et al.,* 2006).

Table 4

Statistical analysis of the obtained results in this study

Cell	Mean value of Azimuth	Dev. from mean (FMSI)	Dev. from mean (SSR)	Dev. from mean (GSR)	Weighted average of Azimuths
4	45.05	1.85	34.45	36.31	45.92
6	42.48	19.88	41.22	21.34	37.33
7	25.38	3.68	19.02	15.33	23.89
8	48.31	49.58	3.12	46.46	46.85
9	148.38	2.32	4.38	2.06	148.93
10	143.81	29.11	27.29	1.81	144.65
11	46.44	27.45	8.15	35.61	49.58
14	26.32	13.02	14.07	1.05	25.84
15	25.08	12.81	18.78	5.97	27.12
16	46.13	4.26	4.46	8.72	47.22
19	36.58	12.38	23.12	10.74	33.70
20	44.78	7.18	27.81	20.62	42.12
23	33.02	14.12	19.48	5.36	31.07
24	72	21.21	16.20	37.41	76.58
25	181.7	11.1	13.1	24.2	178.7
26	19.05	1.09	2.51	1.41	19.81
30	10.26	1.46	0.73	0.73	10.45
31	171.98	1.78	19.28	21.07	171.16
32	168.93	4.86	35.93	31.07	171.04
33	193.93	19.63	22.96	3.3	192.51
34	9.63	1.76	3.86	5.63	10.42
35	9.45	8.95	6.84	2.11	10.26
36	35.93	21.86	7.67	14.19	33.45
39	33.31	5.39	1.29	6.68	33.83
40	53.45	4.85	30.55	25.69	51.41
41	32.83	9.37	6.89	2.48	31.92
43	35.30	7.09	10.20	3.11	34.21
44	43.87	34.03	14.17	19.86	39.73
45	37.27	4.73	1.73	6.46	37.90
48	40.17	26.02	11.87	14.15	36.94
50	51.95	2.46	13.64	11.18	50.95
51	39.25	7.94	2.75	5.19	38.35
53	51.92	9.27	8.87	18.15	54.19

The weighted average Azimuth of compression axis based on focal mechanism stress inversion (FMSI), seismic strain rate (SSR) and geodetic strain rate (GSR), is presented in the last column

The main active shortening in the Zagros is observed in the southeastern part and is taken up by the frontal structures as illustrated in cells 30, 31 and 19 in Fig. (6). According to geodetic measurements, the region northwest of Zagros, (cells 3, 4 and 7), is undergoing relatively less compression and most of the plate deformation due to convergence is transferred northward (WALPERSDORF *et al.,* 2006). Note though that a large compressional seismic strain rate is observed in cell 7, which is associated to past earthquakes in this region (Sahneh earthquake, 13 Dec 1957, M7.1). Low rate of deformation as observed from the geodetic measurements and almost silent seismic deformation in the central part of Iran, roughly defined by cells 27, 28, 22, 8, 13 and 21, supports the idea of the existence of a rigid block in this region. This has also been suggested by other studies (REILINGER *et al.,* 2006; VERNANT *et al.,* 2004a, b). However, one should note that the GPS stations in these cells are not dense enough to reveal possible slow movements along active faults, which have been suggested by JAMALI *et al.* (2011).

The direction of the compressional strain rate components (GSR and SSR) and stress (FMSI) in cells 23 and 26 illustrates the dominant NNE shortening in the southeastern part of Alborz (Figs. 2, 4).

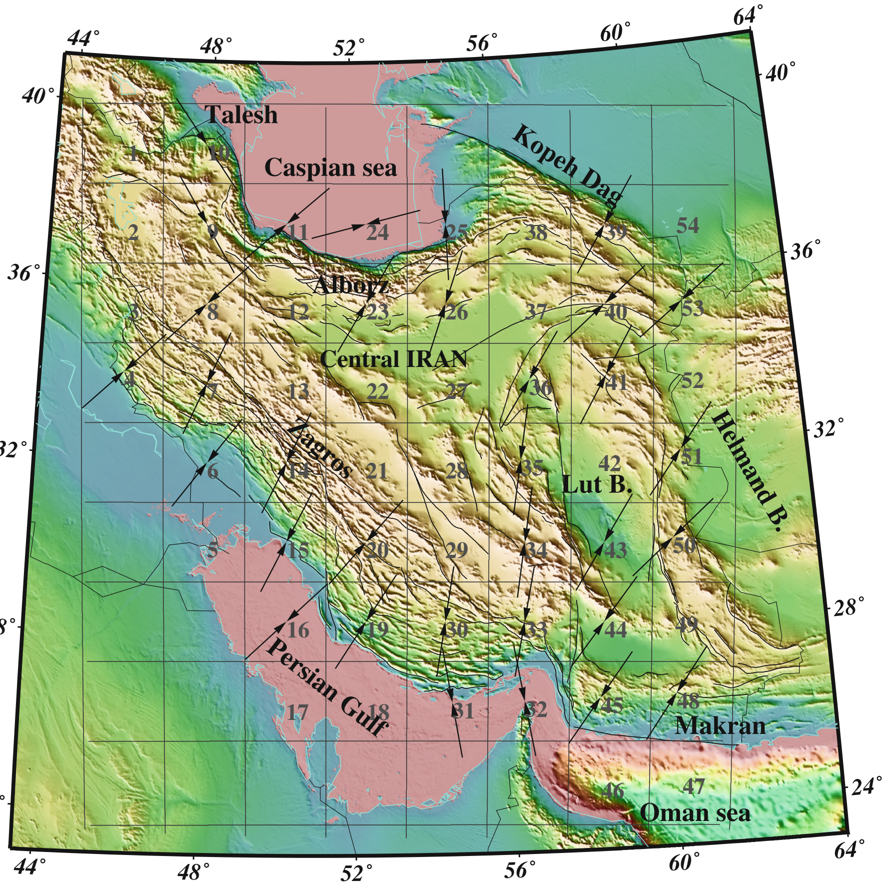

Figure 8

Direction of weighted average maximum horizontal (compressional) stress in Iran, based on results of FMSI, SSR and GSR and Eqs. 5, 6, 7

In the northern Alborz and southern Caspian Sea there is a mismatch in the direction of shortening obtained from seismic data and what has been computed based on geodetic measurements (cells 11, 24 and 25). The gradual change in the direction of compression towards the E–W, based on SSR and FMSI, in the southern Caspian Sea reflects a westward movement of the south Caspian block with respect to Eurasia and Iran, as has been suggested by other researchers (Jackson *et al.*, 2002; Masson *et al.*, 2006). The mismatch with the geodetic measurements in these cells could be related to the relatively short time span during which the geodetic data were collected.

The NNW direction of the principal strain rate and stress axes in cells 1, 2, 9 and 10 (Figs. 3, 4 and 6) represents the changes in the style of deformation in the northwestern part of Iran (close to the Turkish–Iranian border). The extensional components of geodetic strain rate illustrate the change in kinematics in this region, which has been thought to be related partly to strike-slip movements along the North Tabriz fault, to subduction of an old remnant of oceanic crust beneath the Great Caucasus, to westward motion of the south Caspian basin and to active delamination in the lesser Caucasus (Masson *et al.*, 2006; Reilinger *et al.*, 2006; Djamour *et al.*, 2011). The direction of shortening in eastern Iran and Kopeh Dag has a NNE to NE trend. There is a good agreement in direction of shortening between all three methods of investigation in this study. The tectonic forces in Kopeh Dag and eastern Iran are thought to have the same origin. The right lateral shear between central Iran and Afghanistan feeds the shortening in Kopeh Dag and eastern Iran via the N–S right lateral strike slip faults in this region (Lyberis and Manby, 1999; Walker and Jackson, 2004). Such a lateral movement between these two blocks indeed can be the result of a NE and NNE trend of compression. Based on SSR, the dominant compressional deformation in cell 36 has changed to dominant extensional deformation in cell 41. The GSR result also suggests a bigger extensional component of deformation in cell 41, in comparison with cell 36. This may confirm a sharp boundary between central and eastern Iran. The GSR in all cells in central Iran (cells 35, 36 and 37) confirm a smaller component of extension as compared to the neighboring cells in eastern Iran (cells 40, 41 and 42). The high extensional strain component in Kopeh Dag (based on both GSR and SSR) can be explained with the deformation pattern of the Iran–Turan convergence. The 350 km long NW–SE right lateral strike-slip "Ashgabat" fault in Kopeh Dag is representative of the NNE direction of shortening and the NW direction of extension in this region.

We also compared our results with the results presented in the world stress map of Heidbach and Hohne (2008), Heidbach *et al.* (2010), the stress inversion of Gillard and Wyss (1995) in Zagros, Zamani *et al.* (2008) in Kopeh Dag, Zanchi *et al.* (2006) in Alborz and, whenever the comparison was possible (based on the cell allocation), with geodetic studies of Masson *et al.* (2005). We believe there is a good compatibility among these studies and the results of our study. Minor mismatches exist which are caused by differences in the grid size and differences in the number of data used. As observed in our research, different methods of calculations change the results and can generate mismatches even when the same dataset is used. Thus, a stress map obtained using different types of data with a minimum deviation from the average of the stress field obtained in each individual data sets, gives rise to a more realistic stress map.

10. Conclusion

In this study, we have used the long-term seismic activity between 1909 and 2012 and the short-term crustal deformation constrained by geodetic data (1999–2011) to compute the crustal stress field in Iran. The Pearson product moment correlation between the obtained results shows a strong correlation between the directions of principal components of the seismic and geodetic strain rates and stresses. In particular the correlation coefficient of $\rho = +0.84$ between the FMSI and SSR results, the correlation coefficient $\rho = +0.78$ between SSR and GSR and $\rho = +0.79$ between FMSI and GSR (see also Fig. 7) are obtained. These good agreements between the three inversion results are used to compute the stress field using a method based on weighted averages. The new stress field (Fig. 8) is consistent with the tectonic setting of Iran. In particular, this new stress map illustrates the sharp variation in the transition zone between Makran and Zagros, the stress partitioning in northwestern Zagros, the northeastward direction of shortening in Kopeh Dag and eastern Iran, the distinction between the direction of shortening in southern Alborz versus the northern Alborz and south Caspian region and the NW shortening in Talesh and northwestern Iran. This new stress map, obtained using various sources of data and computation methods, with a strong positive correlation between the data and its general agreement with tectonic activity supports the assertion that this stress map provides stable estimates of the state of stress in Iran which should help in further tectonic as well as seismic hazard studies.

Acknowledgments

We are grateful to the associate editor, Eugenio Carminati, and two anonymous reviewers for their useful and constructive comments. ZZ acknowledges supports from the earthquake seismology group at Uppsala University. FN is funded by the Research Council of Sweden (VR). We are grateful to Henk Keers for peer reviewing and editing of our paper. Matlab has been used to develop necessary scripts. GMT, VELROT, SSPX and ZMAP free software/programs were used in this study.

REFERENCES

Allmendinger, R. W., R. Reilinger, and J. Loveless (2007), *Strain and rotation rate from GPS in Tibet, Anatolia, and the Altiplano*, Tectonics, *26*(3), doi:10.1029/2006TC002030.

Allmendinger, R. W., R. Smalley, M. Bevis, H. Caprio, and B. Brooks (2005), *Bending the Bolivian orocline in real time*, Geology, *33*(11), 905–908.

Bayer, R., J. Chery, M. Tatar, P. Vernant, M. Abbassi, F. Masson, E. Nilforoushan, E. Doerflinger, V. Regard, and O. Bellier (2006), *Active deformation in Zagros-Makran transition zone inferred from GPS measurements*, Geophys J Int, *165*(1), 373–381.

Bellahsen, N., C. Faccenna, F. Funiciello, J. M. Daniel, and L. Jolivet (2003), *Why did Arabia separate from Africa? Insights from 3-D laboratory experiments*, Earth Planet Sc Lett, *216*(3), 365–381.

Bhat, H. S., R. Dmowska, J. R. Rice, and N. Kame (2004), *Dynamic slip transfer from the Denali to Totschunda faults, Alaska: Testing theory for fault branching*, B Seismol Soc Am, *94*(6), S202–S213.

Cardozo, N., and R. W. Allmendinger (2009), *SSPX: A program to compute strain from displacement/velocity data*, Comput Geosci-Uk, *35*(6), 1343–1357.

Demets, C., R. G. Gordon, D. F. Argus, and S. Stein (1994), *Effect of Recent Revisions to the Geomagnetic Reversal Time-Scale on Estimates of Current Plate Motions*, Geophys Res Lett, *21*(20), 2191–2194.

Djamour, Y., P. Vernant, H. R. Nankali, and F. Tavakoli (2011), *NW Iran-eastern Turkey present-day kinematics: Results from the Iranian permanent GPS network*, Earth Planet Sc Lett, *307*(1–2), 27–34.

Djamour, Y., *et al.* (2010), *GPS and gravity constraints on continental deformation in the Alborz mountain range, Iran*, Geophys J Int, *183*(3), 1287–1301.

Dong, D., T. A. Herring, and R.W. King (1998), *Estimating regional deformation from a combination of space and terrestrial geodetic data*, J Geodesy, (72), 200–214.

Fliss, S., H. S. Bhat, R. Dmowska, and J. R. Rice (2005), *Fault branching and rupture directivity*, J Geophys Res-Sol Ea, *110*(B6). doi:10.1029/2004JB003368.

Gibons, J. D. (1982), *Nonparametric Statistical Inference*, Second ed.

Gillard, D., and M. Wyss (1995), *Comparison of Strain and Stress Tensor Orientation - Application to Iran and Southern California*, J Geophys Res-Sol Ea, *100*(B11), 22197–22213.

Hatzfeld, D., M. Tatar, K. Priestley, and M. Ghafory-Ashtiany (2003), *Seismological constraints on the crustal structure beneath the Zagros Mountain belt (Iran)*, Geophys J Int, *155*(2), 403–410.

Heidbach, O., and J. Hohne (2008), CASMI: *A visualization tool for the world stress map database*, Comput Geosci-Uk, *34*(7), 783–791.

Heidbach, O., M. Tingay, A. Barth, J. Reinecker, D. Kurfess, and B. Muller (2010), *Global crustal stress pattern based on the World Stress Map database release 2008*, Tectonophysics, *482*(1–4), 3–15.

Herring, T. A., King, R. W., McClusky, S. C. (2010), GLOBK reference manual, global Kalman filter VLBI and GPS analysis program, Release 10.4. Department of Earth, Atmospheric, and Planetary Sciences, MIT, USA, 2010, p. 95.

Hessami, K., F. Nilforoushan, and C. J. Talbot (2006), *Active deformation within the Zagros Mountains deduced from GPS measurements*, J Geol Soc London, *163*, 143–148.

Jackson, J. (1992), *Partitioning of Strike-Slip and Convergent Motion between Eurasia and Arabia in Eastern Turkey and the Caucasus*, J Geophys Res-Sol Ea, *97*(B9), 12471–12479.

Jackson, J., and D. McKenzie (1988), *The Relationship between Plate Motions and Seismic Moment Tensors, and the Rates of Active Deformation in the Mediterranean and Middle-East*, Geophysical Journal-Oxford, *93*(1), 45–73.

Jackson, J., J. Haines, and W. Holt (1994), *A Comparison of Satellite Laser Ranging and Seismicity Data in the Aegean Region*, Geophys Res Lett, *21*(25), 2849–2852.

Jackson, J., J. Haines, and W. Holt (1995), *The Accommodation of Arabia-Eurasia Plate Convergence in Iran*, J Geophys Res-Sol Ea, *100*(B8), 15205–15219.

Jackson, J., K. Priestley, M. Allen, and M. Berberian (2002), *Active tectonics of the South Caspian Basin*, Geophys J Int, *148*(2), 214–245.

Jamali, F., K. Hessami, and M. Ghorashi (2011), *Active tectonics and strain partitioning along dextral fault system in Central Iran: Analysis of geomorphological observations and geophysical data in the Kashan region*, J Asian Earth Sci, *40*(4), 1015–1025.

Kame, N., and T. Yamashita (2003), *Dynamic branching, arresting of rupture and the seismic wave radiation in self-chosen crack path modelling*, Geophys J Int, *155*(3), 1042–1050.

Kame, N., J. R. Rice, and R. Dmowska (2003), *Effects of prestress state and rupture velocity on dynamic fault branching*, J Geophys Res-Sol Ea, *108*(B5), doi:10.1029/2002JB002189.

Kostrov, B. V. (1974), *Seismic moment and energy of earthquakes and seismic flow of rocks*, Phys. Solid Earth, *1*, 23–40.

Kostrov, B. V., and S. Das (2005), *Principles of earthquake source mechanics*, Cambridge Monographs on Mechanics and Applied Mathematics, 288.

Kreemer, C., W. E. Holt, S. Goes, and R. Govers (2000), *Active deformation in eastern Indonesia and the Philippines from GPS and seismicity data*, J Geophys Res-Sol Ea, *105*(B1), 663–680.

Lacombe, O., F. Mouthereau, S. Kargar, and B. Meyer (2006), *Late Cenozoic and modern stress fields in the western Fars (Iran): Implications for the tectonic and kinematic evolution of central Zagros*, Tectonics, *25*(1), doi:10.1029/2005TC001831.

Lyberis, N., and G. Manby (1999), *Oblique to orthogonal convergence across the Turan block in the post-Miocene*, Aapg Bull, *83*(7), 1135–1160.

Masson, F., J. Chery, D. Hatzfeld, J. Martinod, P. Vernant, F. Tavakoli, and M. Ghafory-Ashtiani (2005), *Seismic versus aseismic deformation in Iran inferred from earthquakes and geodetic data*, Geophys J Int, *160*(1), 217–226.

Masson, F., Y. Djamour, S. Van Gorp, J. Chery, M. Tatar, F. Tavakoli, H. Nankali, and P. Vernant (2006), *Extension in NW Iran driven by the motion of the south Caspian basin*, Earth Planet Sc Lett, *252*(1–2), 180–188.

Masson, F., M. Anvari, Y. Djamour, A. Walpersdorf, F. Tavakoli, M. Daignieres, H. Nankali, and S. Van Gorp (2007), *Large-scale velocity field and strain tensor in Iran inferred from GPS measurements: new insight for the present-day deformation pattern within NE Iran*, Geophys J Int, *170*(1), 436–440.

McKenzie, D. P. (1969), *Relation between Fault Plane Solutions for Earthquakes and Directions of Principal Stresses*, B Seismol Soc Am, *59*(2), 591601.

Michael, A. J. (1984), *Determination of Stress from Slip Data - Faults and Folds*, J Geophys Res, *89*(Nb13), 1517–1526.

Michael, A. J. (1987), *Use of Focal Mechanisms to Determine Stress - a Control Study*, J Geophys Res-Solid, *92*(B1), 357–368.

Michael, A. J. (1991), *Spatial Variations in Stress within the 1987 Whittier Narrows, California, Aftershock Sequence - New*

Techniques and Results, J Geophys Res-Solid, *96*(B4), 6303–6319.

Mousavi Z., Walpersdorf A., Walker R.T., Tavakoli F., Pathier E., Nankali H., Nilfouroushan F., Djamour Y., 2013, *Global Positioning System constraints on the active tectonics of NE Iran and the South Caspian region*, Earth and Planetary Science Letters, doi:10.1016/j.epsl.2013.07.007; In press.

Mullick, M., F. Riguzzi, and D. Mukhopadhyay (2009), *Estimates of motion and strain rates across active faults in the frontal part of eastern Himalayas in North Bengal from GPS measurements*, Terra Nova, *21*(5), 410–415.

Navabpour, P., J. Angelier, and E. Barrier (2007), *Cenozoic post-collisional brittle tectonic history and stress reorientation in the High Zagros Belt (Iran, Fars Province)*, Tectonophysics, *432*(1–4), 101–131.

Navabpour, P., J. Angelier, and E. Barrier (2008), *Stress state reconstruction of oblique collision and evolution of deformation partitioning in W-Zagros (Iran, Kermanshah)*, Geophys J Int, *175*(2), 755–782.

Nilforoushan, F., and H. A. Koyi (2007), *Displacement fields and finite strains in a sandbox model simulating a fold-thrust-belt*, Geophys J Int, *169*(3), 1341–1355.

Nilforoushan, F., *et al*. (2003), *GPS network monitors the Arabia-Eurasia collision deformation in Iran*, J Geodesy, *77*(7–8), 411–422.

Nocquet Jean-Mathieu (2012), *Present-day kinematics of the Mediterranean: A comprehensive overview of GPS results*, Tectonophysics, 579, 220–242.

Papazachos, C. B., and A. A. Kiratzi (1992), *A Formulation for Reliable Estimation of Active Crustal Deformation and Its Application to Central Greece*, Geophys J Int, *111*(3), 424–432.

Peyret, M., *et al*. (2009), *Present-day strain distribution across the Minab-Zendan-Palami fault system from dense GPS transects*, Geophys J Int, *179*(2), 751–762.

Poliakov, A. N. B., R. Dmowska, and J. R. Rice (2002), *Dynamic shear rupture interactions with fault bends and off-axis secondary faulting*, J Geophys Res-Sol Ea, *107*(B11), doi:10.1029/2001JB000572.

Regard, V., O. Bellier, J. C. Thomas, M. R. Abbassi, J. Mercier, E. Shabanian, K. Feghhi, and S. Soleymani (2004), *Accommodation of Arabia-Eurasia convergence in the Zagros-Makran transfer zone, SE Iran: A transition between collision and subduction through a young deforming system*, Tectonics, *23*(4), doi:10.1029/2003TC001599.

Reilinger, R., *et al*. (2006), *GPS constraints on continental deformation in the Africa-Arabia-Eurasia continental collision zone and implications for the dynamics of plate interactions*, J Geophys Res-Sol Ea, *111*(B5), doi:10.1029/2005JB004051.

Sowers, J. M., J. R. Unruh, W. R. Lettis, and T. D. Rubin (1994), *Relationship of the Kickapoo Fault to the Johnson Valley and Homestead Valley Faults, San-Bernardino County, California*, B Seismol Soc Am, *84*(3), 528–536.

Stein, S., and M. Wysession (2001), *An introduction to Seismology, Earthquakes and Earth structure*, Blackwell Publishing, 498PP.

Stern, R. J. (2002), *Subduction zones*, Rev Geophys, *40*(4), doi:10.1029/2001RG000108.

Talebian, M., and J. Jackson (2004), *A reappraisal of earthquake focal mechanisms and active shortening in the Zagros mountains of Iran*, Geophys J Int, *156*(3), 506–526.

Tavakoli, F., A. Walpersdorf, C. Authemayou, H. R. Nankali, D. Hatzfeld, M. Tatar, Y. Djamour, F. Nilforoushan, and N. Cotte (2008), *Distribution of the right-lateral strike-slip motion from the Main Recent Fault to the Kazerun Fault System (Zagros, Iran): Evidence from present-day GPS velocities*, Earth Planet Sc Lett, *275*(3–4), 342–347.

Unglert, K., M. K. Savage, N. Fournier, T. Ohkura, and Y. Abe (2011), *Shear wave splitting, v(P)/v(S), and GPS during a time of enhanced activity at Aso caldera, Kyushu*, J Geophys Res-Sol Ea, *116*, doi:10.1029/2011JB008520.

Vernant, P., F. Nilforoushan, J. Chery, R. Bayer, Y. Djamour, F. Masson, H. Nankali, J. F. Ritz, M. Sedighi, and F. Tavakoli (2004), *Deciphering oblique shortening of central Alborz in Iran using geodetic data*, Earth Planet Sc Lett, *223*(1–2), 177–185.

Vernant, P., *et al*. (2004), *Present-day crustal deformation and plate kinematics in the Middle East constrained by GPS measurements in Iran and northern Oman*, Geophys J Int, *157*(1), 381–398.

Walker, R., and J. Jackson (2004), *Active tectonics and late Cenozoic strain distribution in central and eastern Iran*, Tectonics, *23*(5), doi:10.1029/2003TC001529.

Walpersdorf, A., D. Hatzfeld, H. Nankali, F. Tavakoli, F. Nilforoushan, M. Tatar, P. Vernant, J. Chery, and F. Masson (2006), *Difference in the GPS deformation pattern of north and central zagros (Iran),* Geophys J Int, *167*(3), 1077–1088.

Wesnousky, S. G. (2006), *Predicting the endpoints of earthquake ruptures*, Nature, *444*(7117), 358–360.

Wyss, M. (2001), *ZMAP: A tool for analyses of Seismicity Pattern*, ZMAP cook book, ETH, Zurich.

Zamani, B., J. Angelier, and A. Zamani (2008), *State of stress induced by plate convergence and stress partitioning in northeastern Iran, as indicated by focal mechanisms of earthquakes*, J Geodyn, *45*(2–3), 120–132.

Zanchi, A., F. Berra, M. Mattei, M. R. Ghassemi, and J. Sabouri (2006), *Inversion tectonics in central Alborz, Iran*, J Struct Geol, *28*(11), 2023–2037.

Zarifi, Z. (2007) Unusual subduction zones: Case studies in Colombia and Iran, PhD thesis, 226PP.

(Received May 12, 2013, revised August 13, 2013, accepted August 19, 2013, Published online September 27, 2013)